Monitoring the dynamics of cell-derived extracellular vesicles at the nanoscale by liquid-cell transmission electron microscopy

Max Piffoux, Nabeel Ahmad, Jaysen Nelayah, Claire Wilhelm, Amanda Silva, Florence Gazeau, Damien Alloyeau

To cite this version:

Max Piffoux, Nabeel Ahmad, Jaysen Nelayah, Claire Wilhelm, Amanda Silva, et al.. Monitoring the dynamics of cell-derived extracellular vesicles at the nanoscale by liquid-cell transmission electron microscopy. Nanoscale, 2018, 10 (3), pp.1234-1244. 10.1039/C7NR07576F . hal-04277704

HAL Id: hal-04277704
https://hal.science/hal-04277704v1

Monitoring the dynamics of cell-derived extracellular vesicles at the nanoscale by liquid-cell transmission electron microscopy

Max Piffoux,[1,2] *Nabeel Ahmad,*[3] *Jaysen Nelayah,*[3] *Claire Wilhelm,*[1] *Amanda Silva,*[1] *Florence Gazeau,*[1] *Damien Alloyeau.*[3*]

Abstract. Cell-derived extracellular vesicles (EVs) circulating in body fluids hold promises as bioactive therapeutic agents and as biomarkers to diagnose a wide range of diseases. However nano-imaging methods are needed to characterize these complex and heterogeneous soft materials in their native wet environment. Herein, we exploit liquid-cell transmission electron microscopy (LCTEM) to characterize the morphology and dynamic behavior of EVs in physiological media with nanometer resolution. The beam-induced controlled growth of Au nanoparticles on bilayer membranes is used as an original *in situ* staining method to improve the contrast of EVs and artificial liposomes. LCTEM provides information about the size distribution and concentration of EVs that are consistent with Cryo-TEM and nanoparticle tracking analysis measurements. Moreover, LCTEM gives a unique insight into the dynamics of EVs depending on their liquid environment. The size-dependent morphology of EVs is sensitive to osmotic stress which tends to transform their spherical shape to ellipsoidal, stomatocyte or discocyte morphologies. In the liquid-cell, EVs exhibit a sub-diffusive motion due to strong interactions between the Au nanoparticles and the liquid-cell windows. Finally, the high-resolution monitoring of EV aggregation and fusion illustrate that LCTEM opens up a new way to study cell-membrane dynamics.

---

[1] Laboratoire Matière et Systèmes Complexes, UMR7057 CNRS / Université Paris Diderot, Paris France.

[2] Ecole de l'INSERM Lilliane Bettencourt, Paris, France

[3] Laboratoire Matériaux et Phénomènes Quantiques, UMR7162 CNRS / Université Paris Diderot, Paris, France.

[*] corresponding author: damien.alloyeau@univ-paris-diderot.fr;
Tel: +33 1 57 27 69 83; Fax: +33 1 57 27 62 41

Key Words. *In situ* transmission electron microscopy, extracellular vesicles, liposomes, nanoscale imaging, physiological media.

1. Introduction

Dynamical processes of soft and biological matter inherently take place at the nanoscale in liquid. Despite the development of super-resolution fluorescence microscopy overcoming the light diffraction limit, [1] many nanoscale phenomena are still not resolved and their study could benefit from other nanoscale real space imaging method such as electron microscopy. In the last ten years, liquid-cell transmission electron microscopy (LCTEM) has been developed to exploit the high resolution capabilities of transmission electron microscopy (TEM) in controlled liquid environment.[2] Intensively used for probing key nanoscale processes in colloidal chemistry [3-6] and electrochemistry, [7, 8] LCTEM has also emerged as a reliable method to address relevant challenges in life science.[9, 10] This includes, for instance, studying the uptake and biodegradation of nanomaterials in cellular environment, [11, 12] or investigating the native structure of complex biological specimens, ranging from micron-thick cells, [13] to liposomes,[14] bacteria, [15] viruses [16, 17] and nanometric proteins.[18, 19] If the question of biological-cell viability under low-dose electron irradiation is intensively debated, [20-22] it is also essential to determine if the unique combination of spatial and temporal resolution of LCTEM can be exploited to study the dynamic of biological materials at the nanoscale in physiological media.

Extracellular vesicles (EVs) are micro- and nano-scale vesicles delimited by a lipid bilayer membrane that are secreted by every cell types in all body fluids.[23-33] According to their formation and release processes, EVs greatly vary in size and thereby can be classified in the following categories: exosomes (30 - 100 nm), microvesicles (50 - 1000 nm), apoptotic bodies (100 - 5000 nm) or oncosome (1 – 10 µm).[34] Firstly considered as dusts in the blood,[35] these nano-objects have been recognized as potent communication vectors in the organism to deliver information (proteins, RNA, lipids) from a cell to another.[36] Deeply involved in crucial physiological and pathological processes, the potential of EVs raise many promises for the fields of cancerology,[37] immunology,[38] regenerative medicine,[39] as well as for drug delivery.[40] However, both the heterogeneity of EVs and the complexity of methods for EVs detection and characterization make their use in clinical practice a challenge. In particular, characterizing EVs morphology, especially at the nanoscale, remains an unmet need. The material and life sciences communities have concomitantly developed instruments to evaluate the density and size distribution of EVs in conditioned media or native body fluids. Nanoparticle tracking analysis (NTA) is a widely-used method to characterize small EVs (< 500 nm),[41] providing size, concentration and zeta potential measurements of EVs from the analysis of their Brownian motion, while flow cytometry detects larger fluorescent-labeled EVs in clinical samples. [42, 43] Tunable resistive pulse sensing can also be applied to measure the concentration and size of EVs.[44] However, the information provided by these different techniques can be sometimes inconsistent due to the presence of confounding biological entities of similar size such as protein aggregates [45] or immune complexes[46] that co-purify with EVs with various concentrations according to the isolation process.

Hence, direct imaging techniques are needed to distinguish the morphology and reveal the heterogeneity of EVs in their native environments. [47] Moreover the investigation of EVs dynamics would provide crucial information about their generation, fate and interactions with cells. Although dyes and fluorescent proteins have been used to detect EVs by fluorescence microscopy,[48] the structural and morphological studies of EVs remain restricted to atomic force microscopy (AFM) [49] and transmission electron microscopy (TEM).[50] Conventional AFM and TEM allow extracting structural information with sub-nanometer resolution, but it appears that dehydration and fixation processes can drastically affect the morphology of EVs. [51] This artifact was overcome by using cryo-TEM that is now a method of choice to reveal native morphological details or estimate the concentration of EVs in plasma.[52] Nevertheless, freezing processes make dynamic and functional observations impossible.

Here we propose the use of LCTEM together with a novel *in situ* gold staining method in order to explore for the first time the dynamical behavior of artificial and cell-derived EVs in their native state. Beyond studying the size distribution and concentration of EVs, LCTEM reveal how EV morphology depends on their size and on the osmolarity of the environment. We also demonstrate that EV motion in cell culture medium can be monitored by position tracking analysis, showing that diffusion processes are considerably slowed down by strong interactions with the silicon nitride membranes of the liquid cell. Finally, we also highlight promising applications of LCTEM for examining aggregation and fusion between EVs at the nanoscale.

2. Experimental

We used the liquid-cell TEM holder commercialized by Protochips Inc. in which the liquid sample is squeeze in between two silicon wafers called the small and large E-chips (Figure S1a). The gold spacers between the two wafers was 150 nm thick. Each E-chip has a rectangular window covered by a 50 nm thick silicon-nitrite amorphous film. After Ar/O_2 plasma treatment used to make the Echips hydrophilic, the SiN surfaces are assumed to be oxidized. A 2.5 µL droplet of cell medium containing EVs and a micro-molar concentration of chloroauric acid, was deposited on the electron transparent membrane of the small E-chip. The large E-chip was then placed over the small one with their windows in cross-configuration, giving a field of view of roughly 1500 μm^2. The entire chamber was then closed by the lid of the holder tip resulting in a vacuum sealed liquid-cell.

All the *in situ* analyses were realized with an aberration-corrected JEOL ARM 200F microscope equipped with a cold-FEG and operated at 200 kV. LCTEM images and videos were acquired in scanning mode (STEM) on a High-Angular-Annular-Dark-Field (HAADF) detector without changing probe size and condenser aperture in order to maintain a constant beam current (i_e). The latter was measured on a CCD camera prior to insert the sample to determine the dose rate focalized on the liquid cell ($i_e = 5.2 \times 10^7$ electron/s or 8.3 pA). In STEM mode the dose rate is easily controlled since it is inversely proportional to the square of the magnification. With such optical conditions, the dose rate varies from 2.3×10^{-2} to 6 electrons/Å^{2}s, with the magnification used for imaging (from 50k to 800k). 1024*1024 STEM images were recorded with pixel dwell time of 5 µs. EVs dynamics were followed by continuously recording 512×512 STEM images with a very lower pixel dwell time of 1 µs. These conditions reduced the local dose rate but the time resolution of the videos was limited to two frames per second by the recording software (auto-screen recorder). All these experiments were repeated several times to check the reproducibility of the data. We did not use the holder in flow mode, nevertheless, we made sure that the liquid geometry within le liquid-cell was not affected by the formation of radiolyticaly produced H_2 bubbles by observing the whole viewing window in low-magnification mode before and after the observation of EVs. As seen in Figure S1b, the contrast of the window was always characteristic of a fully filled liquid-cell with an outward bowing of the SiN membranes under vacuum. In order to boost the contrast of EVs while maintaining a liquid thickness higher than the size of the vast majority of EVs, all the images and videos were recorded over 12.5 µm^2 areas located 1 µm away from the liquid-cell corners (Figure S1b). Energy-Filtered TEM measurements described in supplementary information (Figure S1c) reveal that the liquid thickness in these areas varies from 185 nm to 350 nm due the outward bowing of the SiN membranes. EV position tracking on LCTEM videos was done using MTrack J plugin of ImageJ.[53]

The classical methods and experimental details about cell culture, production and loading of EVs, preparation of liposomes, cryo-TEM, nanoparticle tracking analysis (NTA) and statistics are described in supplementary information.

3. Results & discussion

3.1. Contrast enhancement and detection of single EVs in cell buffer

We investigated EVs spontaneously released by human endothelial cells (HUVEC) and mesenchymal stem cells (MSC), which are prime candidates for biomarkers and regenerative medicine applications, respectively.[54, 55] Following conventional loading procedure, cell media containing EVs and a micro-molar concentration of chloroauric acid were inserted in a liquid-cell prior to LCTEM analyses (see section 2). In the first seconds of observation, EVs remain undetectable, but the continuous irradiation of a large area of the liquid-cell rapidly leads to the formation of Au nanoparticles (NPs), *via* the reduction of Au precursors by aqueous electron produced by radiolysis. Such electron beam-driven syntheses of metallic nanoparticles has been deeply studied in homogenous aqueous or organic solution [3-6], but remarkably, in cell media, the bilayer membranes act as preferential nucleation sites for the Au NPs. Therefore, a film of percolated Au clusters forms on the EVs (Figures 1a-b) and allows boosting their contrast on images acquired in STEM-HAADF mode. *Ex-situ* analyses performed after unsealing the liquid-cell confirmed the composition of the NPs and provided a precise measurement of their size, ranging from 4 to 8 nm (Figure S2). Interestingly, the growth speed of these metallic layers is easily controllable through the optical parameters of the electron microscope. Indeed, as the concentration of aqueous electrons produced by radiolysis increases with the electron dose rate, the nanoparticle-growth speed increases with the beam current and the magnification. Thus, we defined an experimental protocol in order to observe EVs with sufficient contrast, while avoiding the formation of a thick gold layer on their membrane. As observed in Figure 1a, low dose rate illumination (below 0.1 electron/Å^{2}s) for a few minutes slowly improves the contrast of EVs in the irradiated area, up to a satisfactory level of visibility to study their morphology. EVs of various sizes can then be clearly identified in cell-culture medium (Figure 1b-e). Sub-5 nm resolution is confirmed by the detection of small individual Au NPs when zooming on EV membranes (Figure 1e). As different EVs can be clearly imaged at two specific defocus values, it evidences that they adhere either to the top or the bottom membrane of the liquid-cell. EV membrane are mostly composed by phospholipids and proteins. Nevertheless, this *in situ* staining method was also successfully applied to small unilamellar liposomes comprising only a phospholipid bilayer. The similar contrast-enhancement processes observed on cell-derived and protein-free synthetic vesicles (Figure 1a) reveal that the sites of nucleation of Au NPs are most likely the phospholipids. More importantly, these investigations suggest that this beam-driven NP coating could easily become an efficient generic method to reveal morphological or topological details of a large range of biological specimens and soft materials by LCTEM.

3.2. Structural characterization of EVs in physiological medium

The size distributions of EVs deduced from direct LCTEM observations were compared to NTA measurements performed in the same medium. For two types of EVs produced by HUVEC (Figure 1g) and MSC cells (Figure S3), the size distributions obtained by LCTEM and NTA are in good agreements, with a large majority of EVs around 100 nm, a second peak in the size distribution around 175 - 200 nm, and some rare EVs with a size above 300 nm (Figure S4). EVs derived from MSC and HUVEC were highly similar. The size dispersion of EVs was also deduced from cryo-TEM experiments, in accordance with NTA and LCTEM measurements (Figure 1g). This confirm that the hydrodynamic diameter of EVs measured by NTA in isotopic media is not very different from the diameter defined by their membrane.[56] For Cryo-TEM observations, EVs were previously labeled with 10 - 12 nm Au nanoparticles to facilitate their detection (Figure 1f and Figure S5). This labeling strategy is based on the affinity of Annexin-5 proteins conjugated onto the Au NPs for phosphatidylserine lipids available at the outer layer of the EV membrane. It is worth noting, that we also tried to analyze EVs specifically labeled with Anx5-Au-NPs by LCTEM. However, the Anx5-Au-NPs were systematically observed on the SiN film of the liquid-cell rather than on the EV membranes (Figure 1d). Further works are in progress to make this well-established specific labeling strategy compatible with LCTEM observations. However, only a subset of EV population actually expresses phosphatidylserine.[52] In contrast to Au NP immuno-labeling, our *in situ* non-specific staining method has the ability to reveal the entirety of EVs in liquid cell. This was confirmed by estimating the concentration of EVs measured by LCTEM (20 EVs per μm^3, corresponding roughly to 2×10^{13} EV/ mL) which falls in the same order of magnitude than the one measured by NTA ($8{,}7 \times 10^{12}$ EV/ mL). In line with the high purity ratio of the samples (2×10^{10} particle/microgram of protein,[57] supplementary information), the great majority of biomaterials detected by cryo-TEM and LCTEM display a vesicle-like shape and we observed only very few homogenous aggregates with random shapes that could possibly be due to sample contaminations or protein aggregates. Overall, the consistency of *in situ* TEM measurements with NTA and cryoTEM confirms that LCTEM is an efficient technique to provide quantitative and statistic information about the structure of cell-derived vesicles in their native environment. This important result is also confirmed by the size analysis of liposomes produced by extrusion (114 +/- 27 nm, Figure S6b), because this fabrication method is known to produce liposomes with monodisperse size between 100 and 110 nm.[58]

Since the first TEM pictures of EVs, their morphological characteristics have been matter of debate. For instance, exosomes were initially considered to display a cup-shaped morphology but this observation is now recognized as an artefact due to pre-analytical steps.[51] Herein, we exploited the possibility to visualize single EVs in controlled liquid environment to study how their shape is affected by their size and by the osmotic pressure of the environment. The reduced volume (v) is a commonly used parameter to describe the deformation of vesicles as compared to a perfect sphere.[59] For a vesicle of volume V and surface A, v is given by:

$$v = \frac{V}{{}^{4}\!/_{3}\,\pi R_0^3}$$

with

$$R_0 = \sqrt{\frac{A}{4\pi}}$$

Nevertheless, this relevant parameter which indicates the filling degree of vesicles, cannot be measured on projected TEM images in which the dimensional information along the beam axis is lost. Instead, we characterized EV deformation by measuring the filling degree of their projected shape (S/S_{max}) given by:

$$S/S_{max} = \frac{4\pi S}{P^2}$$

where S and P are the projected surface and perimeter of EVs measured on the images, respectively. Although there is no direct relation between v and S/S_{max}, because this later also depends on the projection angle of EVs, these two parameters decrease when EVs change shape by reducing the inside volume.

As observed in Figure 2, the S/S_{max} ratio of EVs is similar in PBS and HEPES media with an osmolarity of 300 mOsmol/L, the physiological osmolarity of human blood plasma. Under these physiological conditions, small EVs (below 200 nm) mostly display circular projected shape with S/S_{max} ratio close to 1 (Figures 2a, 2b, 2d). The video files in supplementary information show that the circular image of the small EVs does not change when they move. Assuming that this motion also involves the rotation of EVs, we can reasonably conclude that the 3D shape of small EVs is spherical with ν close to 1. Similarly, all the liposomes have a spherical morphology in the liquid-cell (Figure S6c). We also remark that the S/S_{max} ratio decreases when EV size increases (Figures 2d-e), suggesting a tangible ν reduction for larger EVs. This size effect on EV deformation could be explained by intrinsic properties of large EVs with lower surface tension than smaller EVs and/or discrepancies in their membrane composition due to different biogenesis. However the vast majority of EVs observed by Cryo-TEM imaging have a spherical shape in frozen media and no significant variation of S/S_{max} ratio is detected when observing large EVs (Figure 2d-e). This suggests that extrinsic factors, such as the interactions of EVs with the liquid-cell windows may affect the shape of large EVs. Indeed, energy filtered TEM measurements described in supplementary information (Figure S1) demonstrated that the thickness of the liquid film in the observation areas varies from 185 to 350 nm. Therefore, the largest EVs are more prone to interact with the oxidized SiN membranes than smaller EVs. This artifact of LCTEM investigations is also consistent with the thermodynamic calculations of Domitrievski showing that the deformation of lipid vesicles adsorbed on SiO_2 surface is much more pronounced for larger vesicles.[60]

3.3. Deformations of EVs in response to osmotic stress

We then tested the effect of increasing the osmotic concentration of the buffer on the morphology of EVs. Remarkably, the mean S/S_{max} ratio shows a statistically significant decrease from 0,85 to 0,70 when the osmolarity of HEPES medium is increased from 300 mOsmol/L to 750 mOsmol/L (Figure 2f). This expected EV deformation in hyperosmolar media is due the water permeability of natural lipid bilayers that allows water diffusion from the EV interior to the surrounding media to equilibrate the osmotic pressure. Interestingly, as this result was also observed by cryo-TEM (Figure 2f), we can rule out an important interplay of liquid-cell confinement with this response of EVs to osmotic stress. Theoretically, such an increase in osmolarity (x2.5) should reduce v by 60% and S/Smax by 46%, assuming an isotropic deformation. Experimentally, we observe a high dispersion of the S/S_{max} ratio for sub-200 nm vesicles, ranging from 0.28 to 0.92 in hyperosmolar medium (Figure 2d). This heterogeneity in shape can be due to 2D-projection effects due to various orientations of deformed EVs with respect to the electron-beam axis. We can also assume that EVs do not have the same osmotic behavior because of a heterogeneous distribution of their pores and protein channels that can incorporate ionic compounds and equilibrate their osmolarity with the surrounding media.[61]

LCTEM imaging also provides relevant insights into the deformation mechanisms of EVs. Figure 3 exemplifies the variety of shapes observed during the *in situ* observations in liquid medium: (i) round vesicles corresponding to 3D sphere (Figure 3a), (ii) elongated vesicles corresponding to either oblate or prolate ellipsoids (Figure 3b), (iii) elongated vesicles with a concave (stomatocyte) or biconcave (discocyte) surface (Figure 3c). We studied the effects of the size and surrounding osmolarity on this catalog of EV's shapes. We used the S/S_{max} ratio and the solidity (s = area / convex area) as geometric criteria to classify the EV's shapes. As the convex area corresponds to the smallest convex region which contains the EV, $s < 1$ if the EV has concave surfaces. Therefore, EVs are defined as spherical if $S/S_{max} > 0.85$, otherwise they are oblate or prolate if $s > 0.85$ and stomatocyte or discocyte if $s < 0.85$. As observed in Figure 3d, EVs in PBS or HEPES media with physiological osmolarity are mostly spherical (70 – 80%) and the deformed vesicles have essentially oblate/prolate shapes. In hyperosmolar media the proportion of deformed vesicle becomes predominant (75 %) and includes 30 % of stomatocyte/discocyte vesicles. The similar deformation mechanisms observed by LCTEM and Cryo-TEM confirm that the interactions with the liquid-cell membranes, or other possible LCTEM artefacts, do not significantly affect the osmolarity-driven shape transformation of EVs. Although they are far less numerous and more deformed than small EVs in the liquid-cell at physiological osmolarity, large EVs (> 250 nm) observed in hyperosmolar media have similar deformation behavior (Figure 3e). We note that neither vesicles budding nor inclusion of cavities were observed by increasing the osmotic concentration, which is in line with the predictions of the bilayer-coupling model reported by Seifert et al.[59] We did not observed other energetically stable shapes for bilayer vesicles, such as tubular or dumbbell morphologies that closely linked to the budding phenomenon.[52] In contrast with LCTEM observation, the encapsulation of EVs in larger EVs is frequently observed by cryo-TEM (Figures 1f and S5). This discrepancy could be explain by the undetectable contrast of encapsulated EVs on which gold NPs cannot grow if gold precursors cannot cross bilayer membranes.

3.4. Anomalous sub-diffusion of EVs in the liquid cell

LCTEM also provides the possibility to track EV motions in physiological media at the nanoscale. Continuous STEM-HAADF imaging with a frame rate of 2 images per second and a magnification of 50k provides a large enough field of view and suitable spatial and temporal resolutions to quantitatively characterize the mobility of EVs (Figure 4a). Moreover, with these low dose rate conditions (2.3×10^{-2} electron/Å^{2}s), we could not observed further growth of Au NPs over several minutes, meaning that the Au NP coating on EVs is stationary during the time of observation. Under irradiation, EVs start moving on the oxidized SiN film by small sporadic jumps separated by periods of immobility. This discontinuous 2D motion was accompanied by EVs rotation around a given point of their membrane that seems pinned to the SiN membrane. In order to provide insights into EV mobility and interactions with the liquid-cell environment, we tracked the position of 37 EVs for 90 seconds (Figure 4a and video 1 in supplementary information). By measuring the distributions of EV position along the X and Y axes (Figure S7), we can deduce the standard deviation σ of the EV position around their mean position. Comparing σ with the radius R of EVs reveals EVs with very different motilities. Indeed, R / σ varies from 0.1 to 10 and is larger than 1 for 35 % of EVs (Figure 4b). This means that over the 90 seconds of observation some EVs are nearly motionless (they slightly rotate but remains attached to the window), while others explore areas more than 100 times larger than their projected surface. Note that some EVs leave the field of view during the observation so that this exploration area can be even larger.

The relevant average quantity to characterize stochastic movements is the time-averaged mean square displacement MSD given by:

$$MSD(\tau) = \langle \Delta\boldsymbol{r}(\tau)^2 \rangle = \langle (\boldsymbol{r}(t+\tau) - \boldsymbol{r}(t))^2 \rangle$$

where $\mathbf{r}(t)$ is the EV position of the particle at time t, τ is the lag time between two positions taken by the EVs used to calculate the displacement $\Delta\mathbf{r}(\tau)$ and the brackets denote averaging over time. The MSD of Brownian objects in 2 dimensions varies as $4D\tau$, with D the diffusion coefficient that can be calculated by the Stokes-Einstein equation:

$$D = \frac{k_B T}{4\pi\eta R}$$

with k_B the Boltzmann constant, T the temperature, η the viscosity of the diffusion medium and R the radius of the object. Considering T = 25°C, R = 50 nm and η = 0.01 Pa.s, we can compare the time-averaged MSD of single EVs with the theory of Brownian motion for a 100 nm EV in water. As illustrated in Figure 4c, all the considered EVs show a sub-diffusive motion.[62] The restricted space explored by EVs is evidenced by the lag-time dependence of the time and ensemble averaged MSD calculated for 16 trajectories that remain inside the observation area over 90 seconds (Figure 4d). Unlike Brownian diffusion, the time and ensemble averaged MSD saturates with τ and can be approximated with the exponential law: $MSD = \alpha\,(1 - e^{(-\beta\tau)})$ with $\alpha = 5.4 \times 10^{-4}$ and $\beta = 0.18$. Thus the EV excursion is contained in the irradiated area and it is at least 3 orders of magnitude lower than the theoretical Brownian motion of freely moving EVs.

Similar discontinuous 2D movements and reduced mobility have already been reported for the diffusion of nano-objects in a TEM liquid-cell. [63-67] Several explanations have been put forward to account for these slow diffusion processes, including hydrodynamic hindrance near the window's surface,[63, 65] the formation of highly viscous ordered liquid layer, [65, 66] or strong interactions with the liquid-cell windows. [63, 65-67] Electrostatic forces are expected to greatly contribute to these interactions on account of the positive charge of the oxidized SiN membrane under electron irradiation. However, previous LCTEM studies analyzed the diffusion of small metallic NPs. Here, the dynamic behavior of larger biostructures but still coated with Au NPs can provide new insights into the mechanisms slowing down the mobility of nano-objects within the liquid-cell. We used the parameter σ to characterize the mobility of EVs, because the non-linearity of the MSD with τ makes the measurement of diffusion coefficients irrelevant. Unlike metal NPs, [64, 65] the mobility of EVs does not depends on their size (Figure 4e). On the contrary, the EV mobility is significantly affected by the density of Au NPs grafted to their membrane that is directly correlated to their contrast on STEM HAADF images. Indeed, as shown in Figure 4f, σ decreases with increasing EV's signal-to-noise ratio (SNR). The σ of highly contrasted EVs (SNR > 3) that are fully covered by a thick layer of Au NPs (white arrows in Figure 4a) is three time smaller than the σ of poorly contrasted EVs on which Au clusters form a thin and incomplete layer (red arrow in Figure 4a). This suggests that EV mobility is affected by their attractive interactions with the membrane, through the sticking effect of Au NPs. Although we cannot rule out the formation of a viscous ordered liquid layers, such a 5 nm-thick layer could not slow down EVs with sizes ranging from 50 to 600 nm with the same efficiency and it should not be affected by EV coating. On the contrary, the electrostatic attractive force between the EVs and the window varies with the density of positive and negative charges at the SiN and EV surfaces, respectively.

Elucidating the role of the electron beam is also essential to understand the discontinuous diffusion mechanism of EVs. Figure 5a illustrates that the dose rate speeds up the diffusion process by increasing the jump rate of EVs on the window. In this example, the EV makes a single jump of 170 nm in 9 seconds when imaged at 150k magnification (dose rate = 0.2 electrons/$Å^2$s), while it makes 4 jumps and travels 275 nm in only 5 seconds when the magnification is changed to 400k (dose rate = 1.5 electrons/$Å^2$s). Woehl *et al.* have recently proposed that the beam-induced ejection of metallic NPs from the SiN membrane was due to a transfer of the positive charges accumulated in the window to the NPs by contact electrification, followed by a coulombic repulsion of the positively charged NPs which activates their diffusion in the liquid.[67] When the positive charges are released in the buffer, the NPs are attracted again by the membrane and stop diffusing. Following this reasoning, the jump rate of EVs depends on the competition between the attractive interactions with the membrane and electrostatic repulsion. It is worth noting that charge transfer can occurs between silicon oxide and Au in response to unbiased contact.[68] Moreover, recent atomic force microscopy experiments demonstrated that contact electrification process between metallic and dielectric materials can be manipulated both in polarity and magnitude of the charge transfer by applying an electric field between the two materials, which, as the electron beam irradiation, modifies the density of charge in the dielectric media.[69] Therefore we hypothesize that the faster jumping of EVs when the dose rate is increased results from an enhanced transfer of positive charges to the Au NPs due to the higher positive-charge density within the SiN films. Importantly this beam-enhanced diffusion cannot be analysed over a long periods of time because of the growth of the

Au layers at high dose rate, which tend to slow down the EVs until they stop moving (Figure S8). Hence, the tunable density of Au NPs could be an efficient way to modulate the interactions between biostructures and the SiN membranes which can be exploited to tune their diffusion according to whether one is interested in their native structure or their dynamical behavior.

3.5. Aggregation and fusion of EVs

Aggregation is a long standing question in the EV field because their concentration, size or biochemical composition can easily be affected through the formation of aggregates. Due to their negative zeta potential[44] and small size, EVs have been considered for a long time as not subject to aggregation. This assumption was reinforced by the easy dispersion of concentrated pellets after ultracentrifugation. However, Brisson *et al.* recently revealed that ultracentrifugation can induce aggregation processes in human plasma samples.[70] In the liquid-cell, small aggregates of 3 to 5 EVs were found in pristine area (Figure 1c). These aggregates most likely formed during the ultracentrifugation step. Interestingly, we observed sequential attachments of single EVs to existing aggregates (Figure 5b or Video 2 in supplementary information). This diffusion-driven process results in the formation of larger aggregates. The attachment of single EV stops its individual diffusion but the whole aggregate can rotate and slightly diffuse under electron irradiation. This phenomenon confirms that EVs can form small aggregates in solution. However the role of Au NPs remains to be studied because they could promote the attachment of EVs that come into contact. More importantly, LCTEM allowed to monitor some fusion events between EVs into the aggregates. As illustrated in Figure 5c (video 3 in supplementary information), the continuous interface between the two vesicles transform into a fusion pore *via* the merging of the two-bilayer membranes. According to the lipid-lined fusion pore theory, the lipid head-groups from one membrane can spontaneously insert into another membrane if the two membranes are brought to a critical distance.[71] Membrane proximity is usually mediated by SNARE proteins that are not present in the studied EVs. Here, we hypothesize that this condition is enabled by EVs aggregation. This first nanoscale monitoring of vesicle fusion by LCTEM paves the way for further investigations, notably on the role of SNARE complex in the fusion mechanisms or on the release processes of vesicle contents. Interestingly, studying the transfer of internalized nanomaterials from a vesicle to another should allow assessing if the membrane processes observed by LCTEM are a hemi-fusion in which only the outer membranes of the two bilayers merge, or a complete fusion in which the two vesicles share their interior.

4. Conclusion

In conclusion, we summarize the pros, cons and perspectives of this methodology for EVs characterization with respect to other techniques. In first, this work demonstrate that LCTEM together with the *in situ* Au-staining method can be exploited to visualize EVs in their native liquid media with nanometer resolution. Relevant parameters for EV-based diagnostic and therapy, such as the size distribution and concentration can then be extracted and it is even possible to study the equilibrium shape of EVs as a function of the environment composition. Here, morphological analyses in controlled liquid media revealed that the deformation mechanisms in response to osmotic stress tend to transform spherical EVs to ellipsoidal, stomatocyte or discocyte morphologies, but other compositional parameters could be tested. Aside from the deformation of very large EVs that are probably affected by the confined volume of the liquid-cell, all the LCTEM measurements are in line with NTA and cryo-TEM analyses. Therefore, LCTEM turn out to be an easy and practical way to investigate the structural characteristic of EVs at the nanoscale, without freezing the sample. More importantly, this method also open the unique possibility to study the dynamical behavior of EVs. We could then consider studying such deformation processes in real time by modifying the osmotic pressure while observing the EVs. Here, we focused on EVs motion and we demonstrated that they undergo an anomalous sub-diffusion in the liquid-cell that is at least 3 orders of magnitude slower than theoretical Brownian motion, due to strong interactions with the liquid-cell windows. Interestingly, Au NPs play a key role in these interactions which could be efficiently used to control the diffusion of EVs in the liquid-cell. Furthermore, the possibility to monitor aggregation and fusion events with nanometer resolution offers promising perspectives for understanding bilayer-membrane dynamics that plays a central role in cellular processes. The original contrast-enhancement method used here to reveal both cell-derived and artificial vesicles (liposomes), can certainly help visualizing other low-contrast biological materials by LCTEM. Nevertheless, the very likely interplay of gold nanoparticles with the dynamics of biomaterials, as well as the effects of the electron beam (radiolysis and knock-on damages) must be further studied to ensure the bio-physiological relevance of LCTEM investigations.

Conflicts of interest

There are no conflicts of interest to declare.

Acknowledgements

We gratefully acknowledge the help of Alain Brisson and Jean Michel Guigner for the Cryo-TEM analyses and fruitful discussions. We also acknowledge the financial support of the Region Ile-de-France (convention SESAME E1845 for the JEOL ARM 200F electron microscope installed at the Paris Diderot University), the Labex SEAM (Plas-Mag project) and the CNRS (Defi-Nano Program) for the liquid-cell TEM holder. We are also grateful to Ecole Doctorale Frontières du Vivant (Programme Bettencourt), Ecole de l'INSERM - Lilliane Bettencourt and the fondation SERVIER for the financial support of M. Piffoux.

References

1. S. W. Hell and J. Wichmann, *Opt. Lett.*, 1994, **19**, 780-782.
2. M. J. Williamson, R. M. Tromp, P. M. Vereecken, R. Hull and F. M. Ross, *Nat. Mater.*, 2003, **2**, 532-536.
3. H. G. Liao, K. Y. Niu and H. M. Zheng, *Chem. Commun.*, 2013, **49**, 11720-11727.
4. T. J. Woehl, J. E. Evans, I. Arslan, W. D. Ristenpart and N. D. Browning, *Acs Nano*, 2012, **6**, 8599-8610.
5. D. Alloyeau, W. Dachraoui, Y. Javed, H. Belkahla, G. Wang, H. Lecoq, S. Ammar, O. Ersen, A. Wisnet, F. Gazeau and C. Ricolleau, *Nano Lett.*, 2015, **15**, 2574-2581.
6. T. Ngo and H. Yang, *J. Phys. Chem. Lett.*, 2015, **6**, 5051-5061.
7. M. E. Holtz, Y. C. Yu, D. Gunceler, J. Gao, R. Sundararaman, K. A. Schwarz, T. A. Arias, H. D. Abruna and D. A. Muller, *Nano Lett.*, 2014, **14**, 1453-1459.
8. B. L. Mehdi, J. Qian, E. Nasybulin, C. Park, D. A. Welch, R. Faller, H. Mehta, W. A. Henderson, W. Xu, C. M. Wang, J. E. Evans, J. Liu, J. G. Zhang, K. T. Mueller and N. D. Browning, *Nano Lett.*, 2015, **15**, 2168-2173.
9. N. de Jonge and F. M. Ross, *Nat. Nano.*, 2011, **6**, 695-704.
10. F. M. Ross, *Science* 2015, **350**, 1490.
11. D. Elgrabli, W. Dachraoui, C. Menard-Moyon, X. J. Liu, D. Begin, S. Begin-Colin, A. Bianco, F. Gazeau and D. Alloyeau, *Acs Nano*, 2015, **9**, 10113-10124.
12. D. B. Peckys and N. de Jonge, *Nano Lett.*, 2011, **11**, 1733-1738.
13. M. J. Dukes, D. B. Peckys and N. de Jonge, *ACS Nano*, 2010, **4**, 4110-4116.
14. S. M. Hoppe, D. Y. Sasaki, A. N. Kinghorn and K. Hattar, *Langmuir*, 2013, **29**, 9958-9961.
15. T. J. Woehl, S. Kashyap, E. Firlar, T. Perez-Gonzalez, D. Faivre, D. Trubitsyn, D. A. Bazylinski and T. Prozorov, *Scientific Reports*, 2014, **4**, 6854.
16. A. Cameron Varano, A. Rahimi, M. J. Dukes, S. Poelzing, S. M. McDonald and D. F. Kelly, *Chem. Commun.*, 2015, **51**, 16176-16179.
17. J. Park, H. Park, P. Ercius, A. F. Pegoraro, C. Xu, J. W. Kim, S. H. Han and D. A. Weitz, *Nano Lett.*, 2015, **15**, 4737-4744.
18. C. Wang, Q. Qiao, T. Shokuhfar and R. F. Klie, *Advanced Materials*, 2014, **26**, 3410-3414.
19. Utkur M. Mirsaidov, H. Zheng, Y. Casana and P. Matsudaira, *Biophysical Journal*, 2012, **102**, L15-L17.
20. E. Kennedy, E. M. Nelson, T. Tanaka, J. Damiano and G. Timp, *ACS Nano*, 2016, **10**, 2669-2677.
21. N. de Jonge and D. B. Peckys, *ACS Nano*, 2016, **10**, 9061-9063.
22. E. Kennedy, E. M. Nelson, J. Damiano and G. Timp, *ACS Nano*, 2017, **11**, 3-7.
23. N. Blanchard, D. Lankar, F. Faure, A. Regnault, C. Dumont, G. Raposo and C. Hivroz, *J Immunol*, 2002, **168**, 3235-3241.
24. J. Q. Davis, D. Dansereau, R. M. Johnstone and V. Bennett, *J. Biol. Chem.*, 1986, **261**, 15368-15371.
25. H. F. Heijnen, A. E. Schiel, R. Fijnheer, H. J. Geuze and J. J. Sixma, *Blood*, 1999, **94**, 3791-3799.
26. M. J. Martinez-Lorenzo, A. Anel, S. Gamen, I. Monle n, P. Lasierra, L. Larrad, A. Pineiro, M. A. Alava and J. Naval, *J Immunol*, 1999, **163**, 1274-1281.
27. P. J. Peters, H. J. Geuze, H. A. Van der Donk, J. W. Slot, J. M. Griffith, N. J. Stam, H. C. Clevers and J. Borst, *Eur J Immunol*, 1989, **19**, 1469-1475.
28. G. Raposo, D. Tenza, S. Mecheri, R. Peronet, C. Bonnerot and C. Desaymard, *Mol Biol Cell*, 1997, **8**, 2631-2645.

29. D. Skokos, S. Le Panse, I. Villa, J. C. Rousselle, R. Peronet, B. David, A. Namane and S. Mecheri, *J Immunol*, 2001, **166**, 868-876.
30. C. Thery, M. Boussac, P. Veron, P. Ricciardi-Castagnoli, G. Raposo, J. Garin and S. Amigorena, *J Immunol*, 2001, **166**, 7309-7318.
31. C. Thery, A. Regnault, J. Garin, J. Wolfers, L. Zitvogel, P. Ricciardi-Castagnoli, G. Raposo and S. Amigorena, *J. Cell Biol.*, 1999, **147**, 599-610.
32. G. van Niel, G. Raposo, C. Candalh, M. Boussac, R. Hershberg, N. Cerf-Bensussan and M. Heyman, *Gastroenterology*, 2001, **121**, 337-349.
33. L. Zitvogel, A. Regnault, A. Lozier, J. Wolfers, C. Flament, D. Tenza, P. Ricciardi-Castagnoli, G. Raposo and S. Amigorena, *Nat Med*, 1998, **4**, 594-600.
34. M. Yanez-Mo, P. R. Siljander, Z. Andreu, A. B. Zavec, F. E. Borras, E. I. Buzas, K. Buzas, E. Casal, F. Cappello, J. Carvalho, E. Colas, A. Cordeiro-da Silva, S. Fais, J. M. Falcon-Perez, I. M. Ghobrial, B. Giebel, M. Gimona, M. Graner, I. Gursel, M. Gursel, N. H. Heegaard, A. Hendrix, P. Kierulf, K. Kokubun, M. Kosanovic, V. Kralj-Iglic, E. M. Kramer-Albers, S. Laitinen, C. Lasser, T. Lener, E. Ligeti, A. Line, G. Lipps, A. Llorente, J. Lotvall, M. Mancek-Keber, A. Marcilla, M. Mittelbrunn, I. Nazarenko, E. N. Nolte-'t Hoen, T. A. Nyman, L. O'Driscoll, M. Olivan, C. Oliveira, E. Pallinger, H. A. Del Portillo, J. Reventos, M. Rigau, E. Rohde, M. Sammar, F. Sanchez-Madrid, N. Santarem, K. Schallmoser, M. S. Ostenfeld, W. Stoorvogel, R. Stukelj, S. G. Van der Grein, M. H. Vasconcelos, M. H. Wauben and O. De Wever, *J Extracell Vesicles*, 2015, **4**, 27066.
35. P. Wolf, *Br J Haematol*, 1967, **13**, 269-288.
36. M. Simons and G. Raposo, *Curr Opin Cell Biol*, 2009, **21**, 575-581.
37. J. Wolfers, A. Lozier, G. Raposo, A. Regnault, C. Thery, C. Masurier, C. Flament, S. Pouzieux, F. Faure, T. Tursz, E. Angevin, S. Amigorena and L. Zitvogel, *Nat Med*, 2001, **7**, 297-303.
38. G. Raposo, H. W. Nijman, W. Stoorvogel, R. Liejendekker, C. V. Harding, C. J. Melief and H. J. Geuze, *J Exp Med*, 1996, **183**, 1161-1172.
39. J. He, Y. Wang, S. Sun, M. Yu, C. Wang, X. Pei, B. Zhu, J. Wu and W. Zhao, *Nephrology (Carlton)*, 2012, **17**, 493-500.
40. A. K. Silva, J. Kolosnjaj-Tabi, S. Bonneau, I. Marangon, N. Boggetto, K. Aubertin, O. Clement, M. F. Bureau, N. Luciani, F. Gazeau and C. Wilhelm, *ACS Nano*, 2013, **7**, 4954-4966.
41. M. Tong, O. S. Brown, P. R. Stone, L. M. Cree and L. W. Chamley, *Placenta*, 2016, **38**, 29-32.
42. S. L. Maas, J. de Vrij, E. J. van der Vlist, B. Geragousian, L. van Bloois, E. Mastrobattista, R. M. Schiffelers, M. H. Wauben, M. L. Broekman and E. N. Nolte-'t Hoen, *J Control Release*, 2015, **200**, 87-96.
43. V. Pospichalova, J. Svoboda, Z. Dave, A. Kotrbova, K. Kaiser, D. Klemova, L. Ilkovics, A. Hampl, I. Crha, E. Jandakova, L. Minar, V. Weinberger and V. Bryja, *J Extracell Vesicles*, 2015, **4**, 25530.
44. W. Anderson, R. Lane, D. Korbie and M. Trau, *Langmuir*, 2015, **31**, 6577-6587.
45. J. Webber and A. Clayton, *J Extracell Vesicles*, 2013, **2**.
46. B. Gyorgy, K. Modos, E. Pallinger, K. Paloczi, M. Pasztoi, P. Misjak, M. A. Deli, A. Sipos, A. Szalai, I. Voszka, A. Polgar, K. Toth, M. Csete, G. Nagy, S. Gay, A. Falus, A. Kittel and E. I. Buzas, *Blood*, 2011, **117**, e39-48.
47. Y. Wu, W. Deng and D. J. Klinke, 2nd, *Analyst*, 2015, **140**, 6631-6642.
48. T. Tian, Y. L. Zhu, F. H. Hu, Y. Y. Wang, N. P. Huang and Z. D. Xiao, *J. Cell. Physiol.*, 2013, **228**, 1487-1495.
49. S. Sharma, H. I. Rasool, V. Palanisamy, C. Mathisen, M. Schmidt, D. T. Wong and J. K. Gimzewski, *ACS Nano*, 2010, **4**, 1921-1926.
50. F. Momen-Heravi, L. Balaj, S. Alian, J. Tigges, V. Toxavidis, M. Ericsson, R. J. Distel, A. R. Ivanov, J. Skog and W. P. Kuo, *Front Physiol*, 2012, **3**, 354.
51. C. Théry, S. Amigorena, G. Raposo and A. Clayton, *Curr. Protoc. Cell Biol.*, 2006, **30**, unit 3.32.
52. N. Arraud, R. Linares, S. Tan, C. Gounou, J. M. Pasquet, S. Mornet and A. R. Brisson, *J Thromb Haemost*, 2014, **12**, 614-627.

53. E. Meijering, O. Dzyubachyk and I. Smal, *Methods Enzymol.*, 2012, **504**, 183-200.
54. C. Hromada, S. Mühleder, J. Grillari, H. Redl and W. Holnthoner, *Frontiers in Physiology*, 2017, **8**, 275.
55. D. G. Phinney and M. F. Pittenger, *STEM CELLS*, 2017, **35**, 851-858.
56. N. Llorret, R. Frederiksen, T. Møller, N. Rieben, S. Upadhyay, L. De Vico, J. Jensen, J. Nygård and K. Martinez, *Nanotechnology*, 2013, **24**, 035501.
57. J. Webber and A. Clayton, *Journal of Extracellular Vesicles*, 2013, **2**, 19861.
58. A. Hinna, F. Steiniger, S. Hupfeld, P. Stein, J. Kuntsche and M. Brandl, *J. Liposome Res.*, 2016, **26**, 11-20.
59. U. Seifert, K. Berndl and R. Lipowsky, *Phys Rev A*, 1991, **44**, 1182-1202.
60. K. Dimitrievski, *Langmuir*, 2010, **26**, 3008-3011.
61. K. Strange, *J. Am. Soc. Nephr.*, 1992, **3**, 12-27.
62. S. Havlin and D. Ben-Avraham, *Advances in Physics*, 2002, **51**, 187-292.
63. E. R. White, M. Mecklenburg, B. Shevitski, S. B. Singer and B. C. Regan, *Langmuir*, 2012, **28**, 3695-3698.
64. H. Zheng, S. A. Claridge, A. M. Minor, A. P. Alivisatos and U. Dahmen, *Nano Lett.*, 2009, **9**, 2460-2465.
65. J. Lu, Z. Aabdin, N. D. Loh, D. Bhattacharya and U. Mirsaidov, *Nano Lett.*, 2014, **14**, 2111-2115.
66. A. Verch, M. Pfaff and N. de Jonge, *Langmuir*, 2015, **31**, 6956-6964.
67. T. J. Woehl and T. Prozorov, *J. Phys. Chem. C*, 2015, **119**, 21261-21269.
68. S. Cunningham, *Journal of Electrostatics*, 1997, **40**, 225-230.
69. Y. S. Zhou, S. Wang, Y. Yang, G. Zhu, S. Niu, Z.-H. Lin, Y. Liu and Z. L. Wang, *Nano Lett.*, 2014, **14**, 1567-1572.
70. R. Linares, S. Tan, C. Gounou, N. Arraud and A. R. Brisson, *J Extracell Vesicles*, 2015, **4**, 29509.
71. S. J. Marrink and A. E. Mark, *J. Am. Chem. Soc.*, 2003, **125**, 11144-11145.

Figures

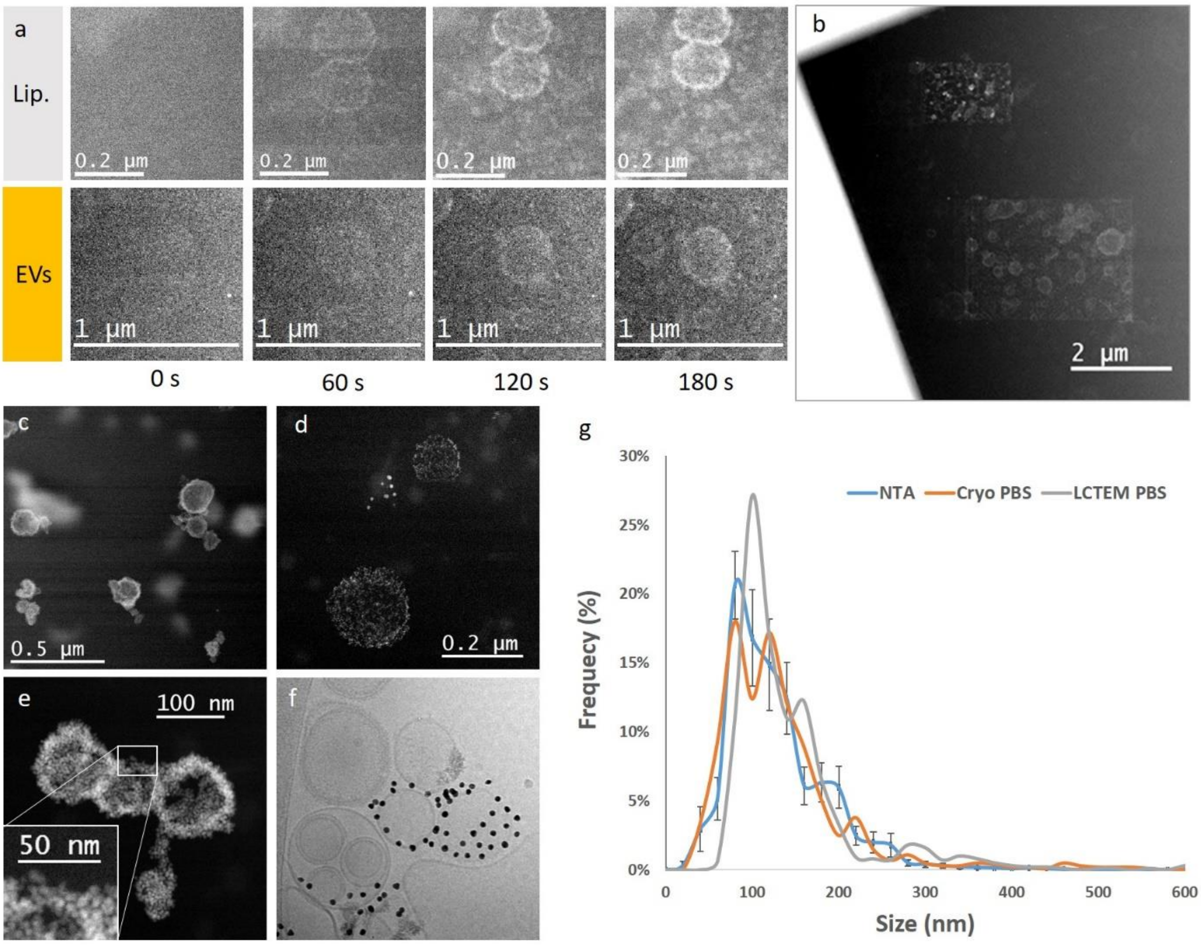

Figure 1. Imaging EVs produced by HUVEC cells in HEPES medium. (a) Image series showing the *in situ* staining of synthetic liposomes (top) and EVs (bottom) *via* the beam-induced growth of Au nanoparticles on their membranes (the observation time is indicated below the images). (b) Low-magnification picture of an EV sample showing the *in situ* labeling of two areas irradiated with different times and intensity, surrounded by non-irradiated zones in which vesicles are not visible (c-e) LCTEM images acquired in STEM HAADF mode of EVs in HEPES buffer stained with Au NPs. The magnified image in insert in (e) shows percolated Au NPs on the vesicle membrane. (f) Bright field Cryo-TEM image of EVs in HEPES. White and red arrows indicate calcium-phosphate nanocrystals and Au NPs conjugated with Annexin-A5 proteins, respectively. (g) Size distribution of EVs obtained by NTA, LCTEM (n = 218) and cryo-TEM (n = 145).

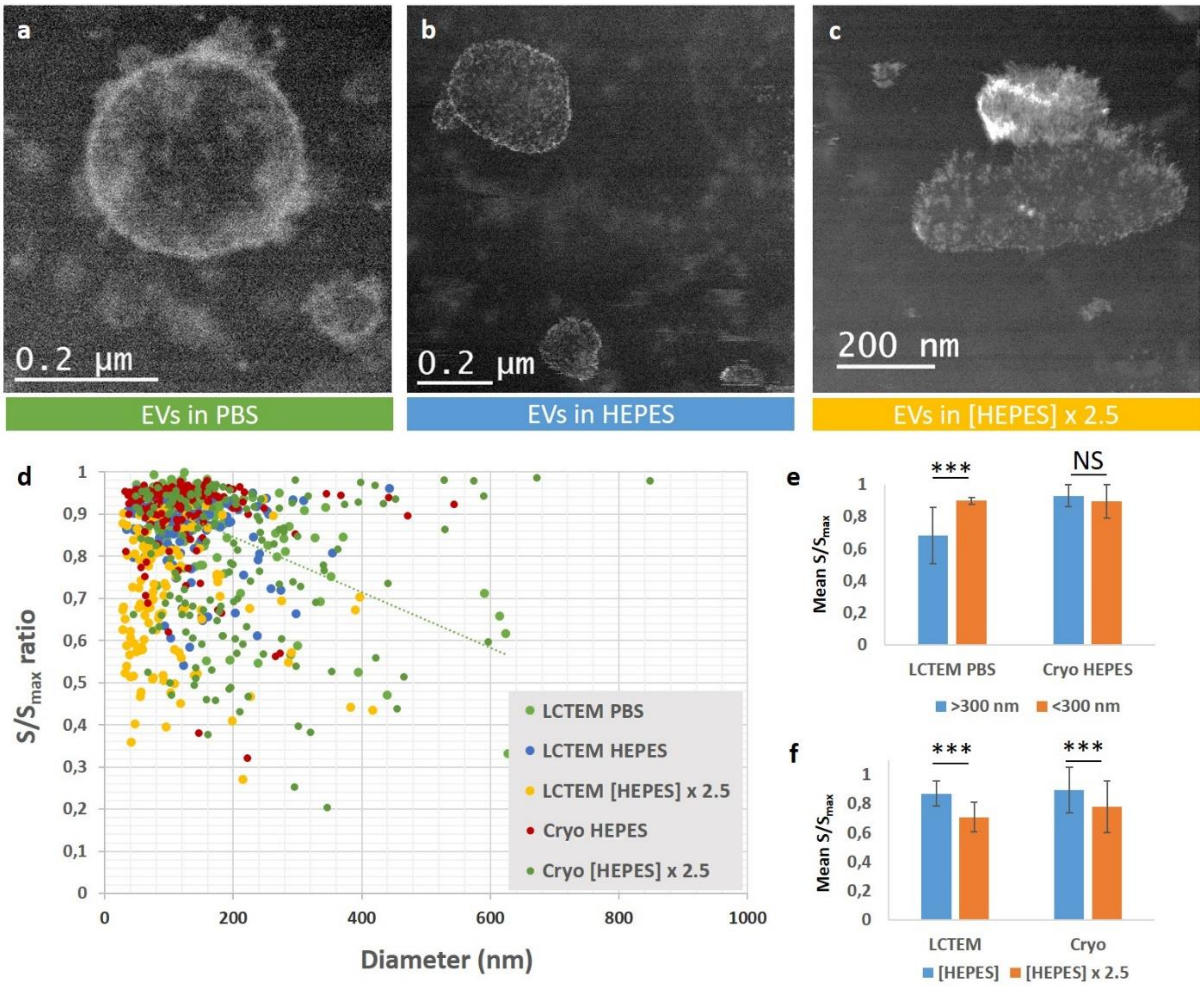

Figure 2. Effects of the size and osmotic concentration on EV's shape. (a,b,c) Representative LCTEM pictures of EV in PBS (300 mOsmol/L), HEPES (300 mOsmol/L), hyperosmolar HEPES x 2.5 (750 mOsmol/L) media, respectively. (d) S/S_{max} ratio plotted as a function of the diameter of EVs measured by LCTEM in PBS, in HEPES and HEPES x 2.5 media and by Cryo-TEM in HEPES and HEPES x 2.5. (e) Mean S/S_{max} ratio measured by LCTEM in PBS and by Cryo-TEM in HEPES for small (< 300 nm, $n_{LCTEM} = 205$; $n_{cryo} = 140$) and large (> 300 nm, $n_{LCTEM} = 13$; $n_{cryo} = 5$) EVs. (f) Mean S/S_{max} ratio of EVs measured by LCTEM and Cryo-TEM in HEPES ($n_{LCTEM} = 148$; $n_{cryo} = 145$) and hyperosmolar HEPES x 2.5 media ($n_{LCTEM} = 130$; $n_{cryo} = 160$). *** Designate a statistically-significant difference between the two groups ($p < 0.001$), NS designate a statistically-insignificant difference ($p > 0.05$)

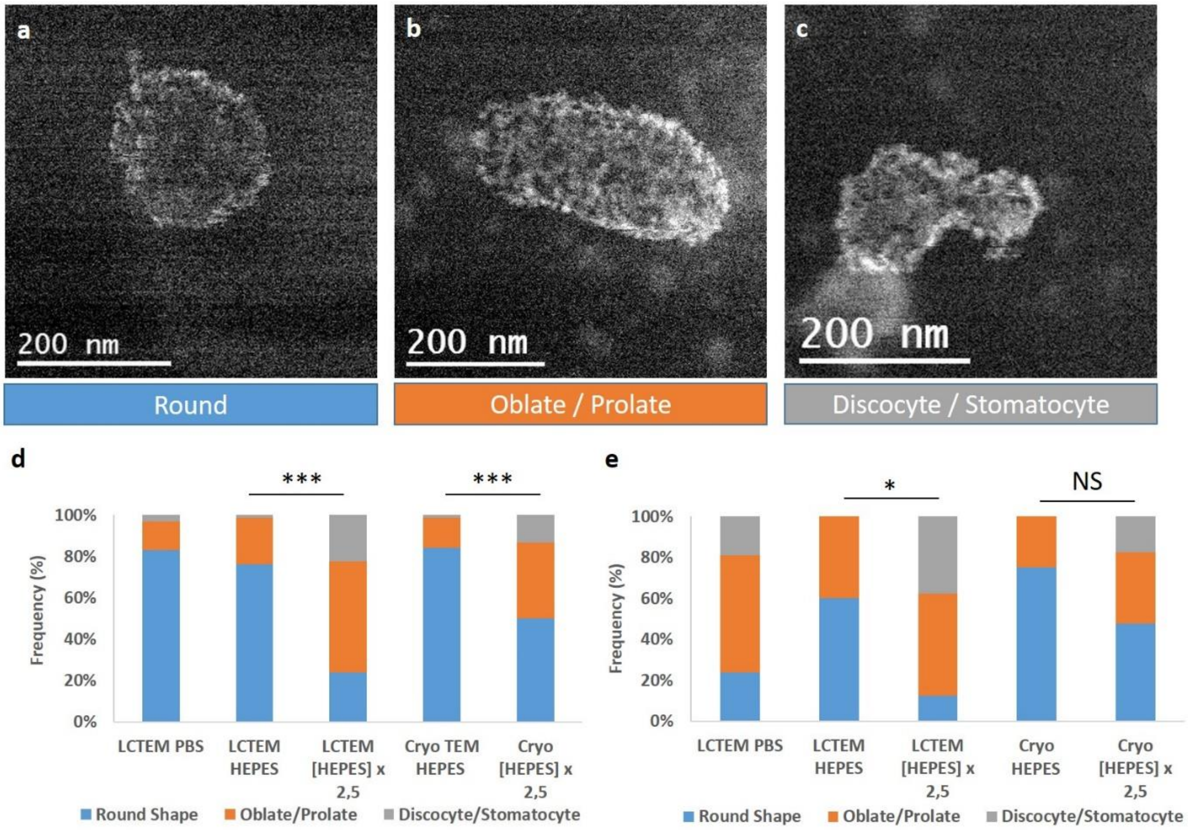

Figure 3. Deformation mechanisms of EVs. (a,b,c) Representative LCTEM pictures of a round EVs, an oblate (or prolate) EVs and a discocyte EVs, respectively. Respective percentage of round (blue), oblate / prolate (orange) and stomatocyte / discocyte EVs (grey), measured in liquid PBS, HEPES and hyperosmolar HEPES by LCTEM and in frozen HEPES and frozen hyperosmolar HEPES by cryo-TEM. (d) Measurements for all EVs. (e) Measurements for EVs larger than 250 nm. *** Designate a statistically-significant difference between the two groups ($p < 0.001$), * designate a statistically-significant difference between the two groups ($p < 0.05$), NS designate a statistically-insignificant difference ($p > 0.05$).

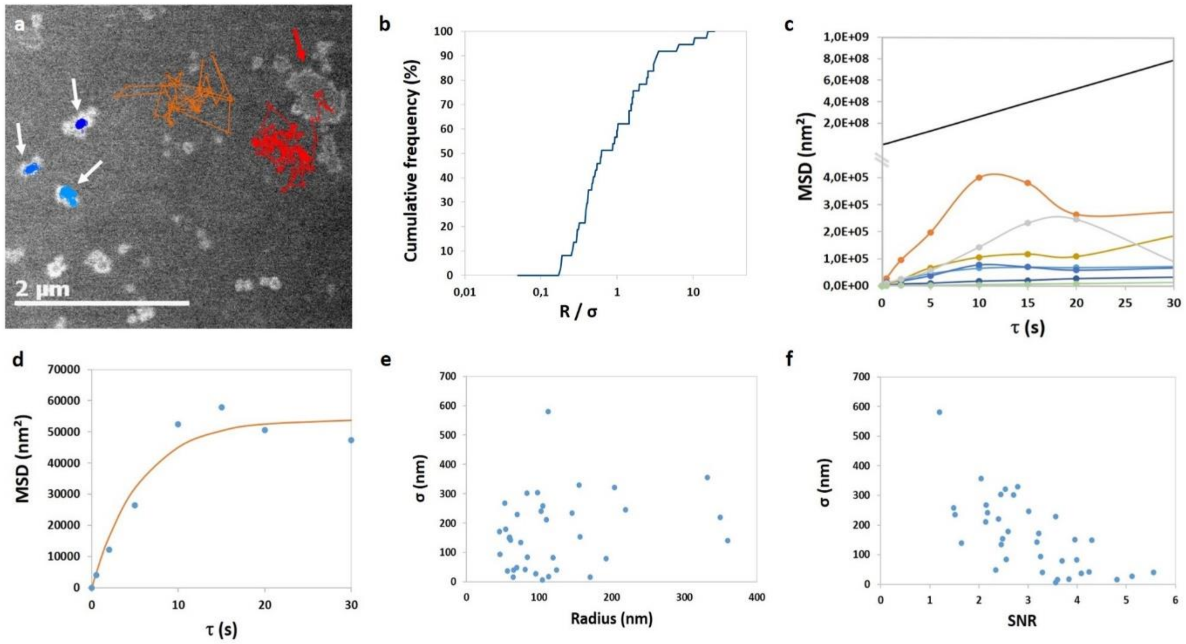

Figure 4. Diffusion of EVs in the liquid-cell studied by position tracking analysis. (a) LCTEM image of EVs in PBS showing the diffusion pathways of several EVs measured over 90 seconds. White arrows highlight highly contrasted EVs with a very restricted motion and the red arrow indicates a low contrast EV with a high mobility. The 90 seconds video used for the measurements can be seen in supplementary information (video 1). (b) Cumulative frequency of EVs as a function of the ratio between their Radius (R) and the standard deviation of their position around their mean position (σ). (c) Time-averaged MSD of 5 singles EVs as a function of the lag time used between two position measurements. The black curved shows the theoretical Brownian motion of a nano-object with a 50 nm radius in water at 25°C (η = 0.01 Pa.s). Note the discontinuity in the Y axis scale. (d) Time and ensemble averaged MSD calculated over 16 trajectories as a function of the lag time. Experimental data are fitted with an exponential law: $MSD = \alpha\ (1 - e^{(-\beta\tau)})$ with $\alpha = 5.4\ 10^{-4}$ and $\beta = 0.18$. (e, f) σ as a function of the EV radius and signal to noise ratio (SNR), respectively.

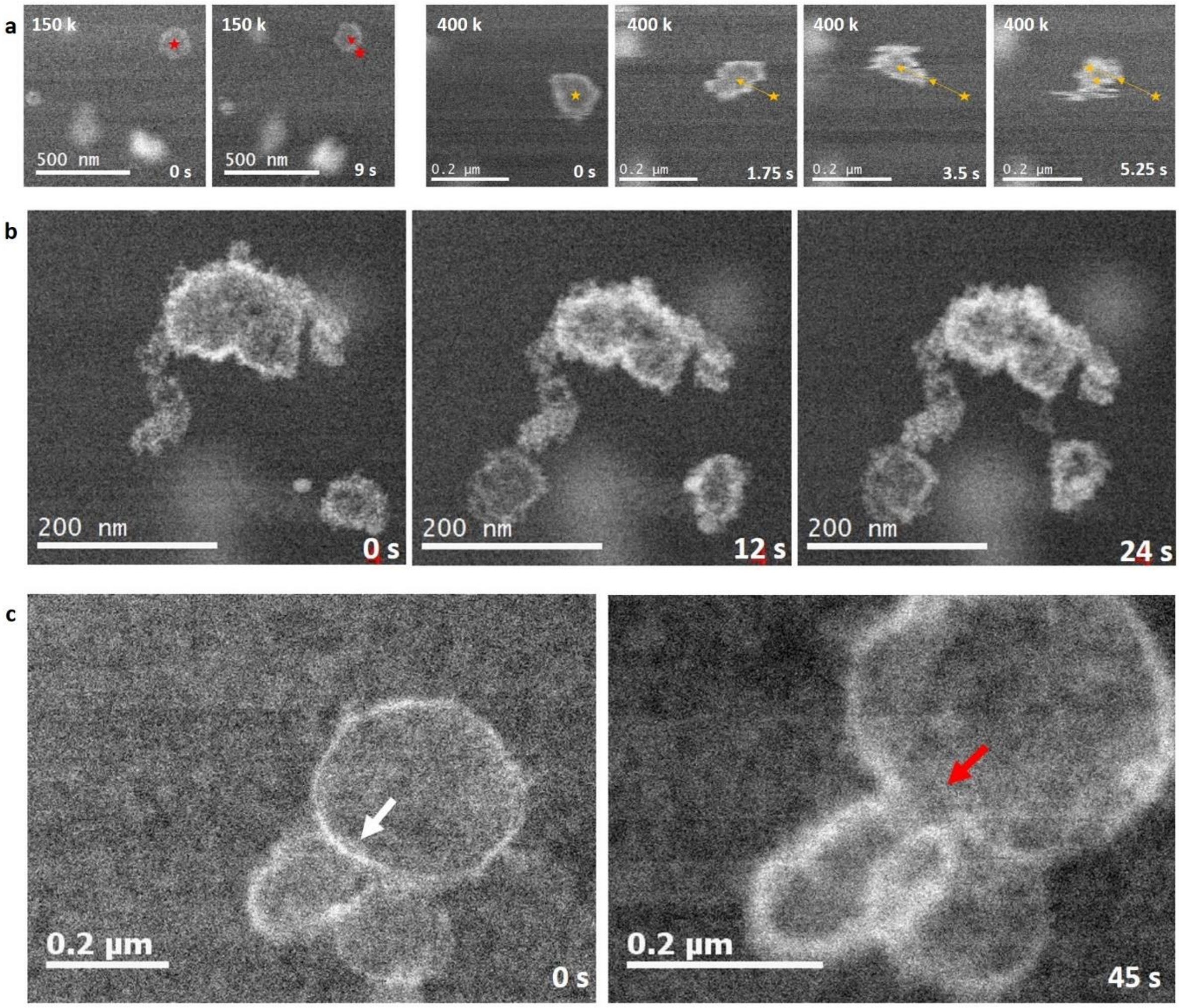

Figure 5. Beam-induced mobility and interaction between EVs. LCTEM images of EVs extracted from video files (the observation time is indicated in the bottom-right corner of each image). (a) The star show the initial position of the EV and the arrows show the diffusion pathway of the EV from frame to frame. As indicated in the top left corner of each image the magnification was changed from 150 k (dose rate = 2 electrons/Å^{2}s) to 400 k (dose rate = 14.2 electrons/Å^{2}s) between the second and the third image of the series. Experiment done in HEPES. (b) Diffusion and aggregation of EVs that tend to form elongated structure in HEPES. (c) Fusion of aggregated EVs produced by MSC cells and dispersed in RPMI media. The white arrow on the first image highlights the continuous interface between the two vesicles. The red arrow on the second image indicates the formation a fusion pore *via* the merging of the two-bilayer membranes. Videos corresponding to images (b) and (c) can be seen in supplementary information (video 2 and 3, respectively).

Graphical abstract

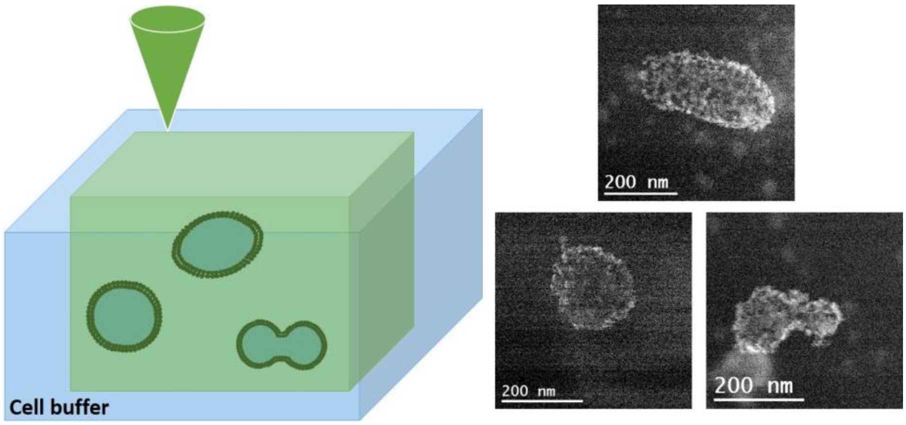

Visualizing the behavior of extracellular vesicles and synthetic liposomes in their native environement at the nanoscale.